Int. J. Heat Mass Transfer. Vol. 30, No. 1, pp. 151–164, 1987
Printed in Great Britain

0017–9310/87 $3.00 + 0.00
Pergamon Journals Ltd.

Mixed convection in vertical, cylindrical annuli

M. A. HESSAMI,* G. DE VAHL DAVIS,† E. LEONARDI and J. A. REIZES
School of Mechanical and Industrial Engineering, University of New South Wales, Kensington, NSW, Australia 2033

(*Received* 22 *January* 1986 *and in final form* 12 *March* 1986)

Abstract—The laminar flow patterns and heat transfer for air contained in the enclosure formed between two vertical, concentric cylinders and two horizontal planes have been studied numerically. The inner cylinder and one of the horizontal planes are heated and rotated about the vertical axis; the other horizontal plane and outer cylinder are cooled and kept stationary. This geometry simulates the gaps at the ends of the rotor of a small, air-cooled, vertically mounted electric motor. The results facilitate the thermal design of such a motor.

The influences of geometry (described by the radius ratio R and aspect ratio A), Ra and Re on temperature and velocity distributions have been investigated. Solutions have been obtained for $0.25 \leqslant A \leqslant 4.0$, $1.2 \leqslant R \leqslant 8.0$, $10 \leqslant Re \leqslant 300$ and $10^3 \leqslant Ra \leqslant 10^5$. It has been found that for low values of R and high values of Re the flow is dominated by centrifugal forces, whereas for high A and Ra buoyancy effects determine the flow patterns and, therefore, the heat transfer. Monocellular flow patterns have been found for the cases where one of these forces is dominant; otherwise two- or three-cell structures have been obtained.

1. INTRODUCTION

HEAT transfer in cylindrical cavities is of particular interest to industry in the design of various types of machinery which involve heating and/or cooling. An example of such equipment is a rotating electric motor which is heated by the bearing friction losses and the ohmic dissipation of electric energy in the windings, and is cooled by the convection of heat from the surface to the surrounding fluid. This process of heating and cooling of the electric motor may induce uneven thermal stresses which can shorten the useful life of the machine. In order to improve the design of such equipment and hence minimize possible failures, a better knowledge of heat transfer from, and flow patterns inside the device is necessary.

The annular cavities at the two ends of the rotor of a vertically mounted electric motor (Fig. 1a) are the critical regions around the rotor due to the presence of relatively higher temperature gradients; the study of heat transfer and flow patterns inside these cavities is the subject of this paper. This annular geometry is formed by two vertical concentric circular cylinders and two horizontal planes, as shown in Fig. 1b. The rotating inner cylinder of radius r_i' and surface temperature T_i' represents the shaft of the heated electric motor surrounded by air and enclosed by the stationary outer casing of radius r_o' and surface temperature T_o' ($< T_i'$) and the horizontal end plates. When the bottom surface of the cavity is heated and rotating, the cavity represents the gap between the upper end of the rotor and the casing (hereafter called the upper annulus); however, with the upper surface heated and rotated, the cavity simulates the gap at the lower end of the rotor (hereafter called the lower annulus). The size of the enclosure is described by the dimensionless radius ratio R and aspect ratio A.

This problem was first studied by de Vahl Davis *et al.* [1] who investigated numerically the effects of Ra and Re on the flow inside a vertical, cylindrical annulus with an aspect ratio of 1.0 and radius ratio of 2.0. No other study (experimental or theoretical) of this problem has been reported in the literature. However, similar problems have received some attention and are briefly reviewed here.

Conlisk and Walker [2] looked at the forced convection in a rapidly rotating, vertical, cylindrical annulus, and investigated the effects of injection and suction on the flow pattern and heat transfer. The thermal boundary conditions considered by them were adiabatic inner and outer cylinders, and hotter upper end plate as compared to the lower one. Singh and Rajvanshi [3] reported the results of their analytical study of heat transfer between rotating eccentric cylinders (each one moving at a different speed) with different radii, using $T_i > T_o$. Buhler and Oertel [4] studied the cell structure in rotating rectangular boxes by experimental and theoretical approaches. Similarly, Charmchi and Sparrow [5] and Sparrow and Charmchi [6] studied the heat transfer and flow pattern in the cavity between two concentric, vertical cylinders; the inner cylinder of smaller height (and diameter) was considered to have been placed at various axial locations. Lastly, Young and Ulrich [7] studied mixed convective heat transfer from a vertical, heated cylinder in a cross-flow; the heat transfer data were correlated by including the influence of Re, Ra and the aspect ratio of the cylinder.

* Now at Research and Technology Centre, Coated Products Division, BHP Steel International Group, Port Kembla, NSW, Australia.
† To whom correspondence should be addressed.

NOMENCLATURE

A	aspect ratio, H'/L'
c_k	constants
C'_p	specific heat at constant pressure
F'	body force per unit mass
Fr	Froude number, $L'\Omega'^2/g'$
g'	gravitational acceleration
Gr	Grashof number, $g'\beta'L'^3\Delta T'/\nu'^2$
h'	coefficient of heat transfer
H'	height of the annulus
k'	thermal conductivity
L'	gap width, $r'_o - r'_i$
Nu	Nusselt number, $h'L'/k'$
p'	pressure
Pr	Prandtl number, $C'_p\mu'/k'$
r'	radial coordinate
r'_i	radius of the inner cylinder
r'_o	radius of the outer cylinder
R	radius ratio, r'_o/r'_i
Ra	Rayleigh number, $PrGr$
Re	Reynolds number, $L'^2\Omega'/\nu'$
S	area
t'	time
T'	temperature
u'	velocity in r' direction
v'	velocity in ϕ' direction
w'	velocity in z' direction
z'	axial coordinate.

Greek symbols

β'	volumetric coefficient of thermal expansion
Δ	change of
Γ'	swirl velocity, $v'r'$
μ'	dynamic viscosity
ν'	kinematic viscosity, μ'/ρ'
Ω'	angular velocity of the rotating cylinder
ϕ'	angular coordinate
ρ'	density
ψ'	stream function, equation (4)
θ	dimensionless temperature [equation (3)]
ζ'	vorticity.

Subscripts

b	boundary
i	inner cylinder
k	an integer ($1 \leqq k \leqq 5$)
L	lower annulus
max	maximum value
o	outer cylinder
T	total
U	upper annulus.

Other symbols

$'$	dimensional quantity
$\bar{}$	an average value.

The present research was undertaken to continue the work reported by de Vahl Davis *et al.* [1] by studying the effects of geometry (i.e. A and R) at various Ra and Re on the flow pattern and heat transfer. The ranges of parameters considered in this study were $1.2 \leqslant R \leqslant 8.0$, $0.25 \leqslant A \leqslant 4.0$, $10^3 \leqslant Ra \leqslant 10^5$, and $10 \leqslant Re \leqslant 300$. These are typical of the prototype electric motor problems: a cavity

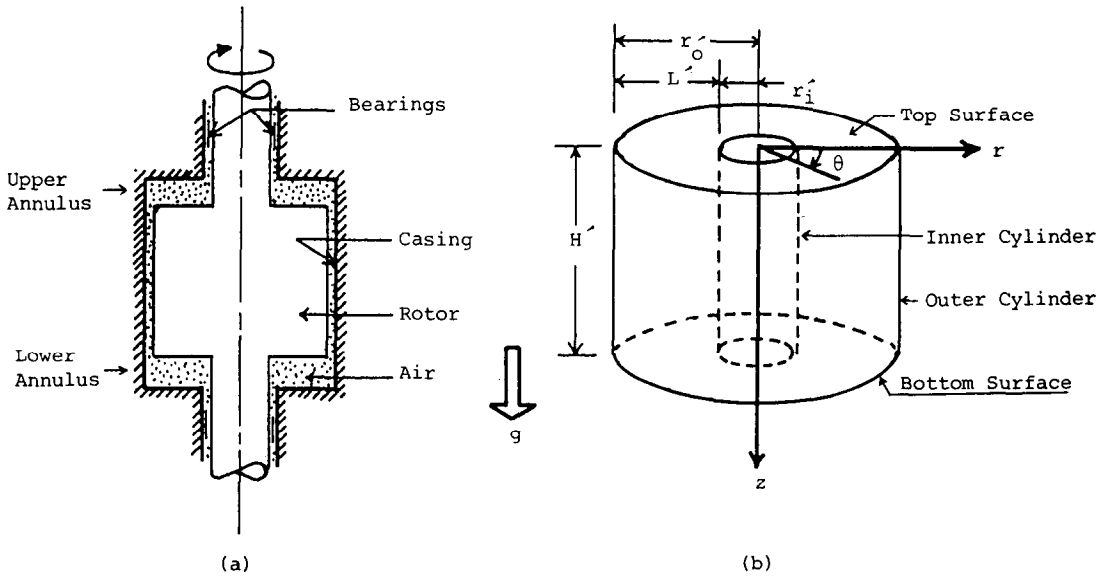

FIG. 1. The geometry and coordinate system. (a) Schematic diagram of an electric motor. (b) Schematic diagram of a vertical annular cavity.

with a gap width of 10 mm, rotating at 500 r.p.m. and experiencing a temperature difference of 60°C across the annular gap operates at approximately $Re = 300$ and $Ra = 5 \times 10^3$ which falls within the range of the parameters considered here.

The computations involved solving the two-dimensional governing differential equations for laminar flow when expressed in terms of the derived variables, i.e. ψ, ζ and Γ; the false-transient method with an ADI scheme was used. The differential equations were simplified using the Boussinesq approximation.

2. MATHEMATICAL FORMULATION

2.1. *The governing differential equations*

The flow inside the cylindrical cavity shown in Fig. 1 can be mathematically described by the continuity, momentum and energy equations. These equations in their general form are parabolic (or, as $t' \to \infty$, may become elliptic), non-linear and coupled; their analytical solution is impossible and a full numerical solution is complicated and time consuming. Here, vertically mounted electric motors are considered so that the gravitational force is independent of ϕ and the flow is two-dimensional. In addition, for air over the temperature ranges likely to be encountered, the fluid properties may be assumed constant except for the density in body force terms. The body forces considered here are those due to gravitational buoyancy, and centrifugal and Coriolis accelerations. Also, the dissipation factor and work of compression are assumed to be zero. Therefore, the governing differential equations in terms of the primitive variables are:

$$\partial u'/\partial r' + \partial w'/\partial z' + u'/r' = 0 \tag{1a}$$

$$\begin{aligned}\partial u'/\partial t' + u'\partial u'/\partial r' + w'\partial u'/\partial z' &= (\rho'/\rho_o')F_r' + (\mu'/\rho_o')[2\partial^2 u'/\partial r'^2 \\ &+ \partial(\partial u'/\partial z' + \partial w'/\partial r')/\partial z' + 2(\partial u'/\partial r' \\ &- u'/r')/r'] - (1/\rho_o')\partial p'/\partial r'\end{aligned} \tag{1b}$$

$$\begin{aligned}\partial v'/\partial t' + u'\partial v'/\partial r' + w'\partial v'/\partial z' + (\rho'/\rho_o')u'v'/r' &= (\mu'/\rho_o')[\partial(\partial v'/\partial r' - v'/r')/\partial r' \\ &+ \partial^2 v'/\partial z'^2 + (2/r')(\partial v'/\partial r' - v'/r')]\end{aligned} \tag{1c}$$

$$\begin{aligned}\partial w'/\partial t' + u'\partial w'/\partial r' + w'\partial w'/\partial z' &= (\rho'/\rho_o')F_z' - (1/\rho_o')\partial p'/\partial z' \\ &+ (\mu'/\rho_o')[2\partial^2 w'/\partial z'^2 + \partial(\partial u'/\partial z' \\ &+ \partial w'/\partial r')/\partial r' + (1/r')(\partial u'/\partial z' + \partial w'/\partial r')]\end{aligned} \tag{1d}$$

$$\begin{aligned}\partial T'/\partial t' + u'\partial T'/\partial r' + w'\partial T'/\partial z' &= k'/(\rho_o' C_p')[(1/r')\partial(r'\partial T'/\partial r')/\partial r' + \partial^2 T'/\partial z'^2]\end{aligned} \tag{1e}$$

where ρ_o' is the density of the fluid at a reference temperature (e.g. T_o') and F' is the body force per unit mass: $F_r' = v'^2/r'$ and $F_z' = g'$ are the centrifugal and gravitational accelerations, respectively; the Coriolis acceleration is represented by $u'v'/r'$ in equation (1c).

A linear variation between density (ρ') and temperature (T') has been assumed:

$$\rho' = \rho_o'[1 - \beta'(T' - T_o')]. \tag{2}$$

The above equations can be non-dimensionalized using the following scales: L' for length; $1/\Omega'$ for time; $L'\Omega'$ for velocity; $\rho_o'(L'\Omega')^2$ for pressure; and $(T_i' - T_o')$ for temperature. It is convenient to use $(T' - T_o')$ instead of T' so that the resulting dimensionless temperature (θ) will be in the range $0 \leqslant \theta \leqslant 1$, i.e.

$$\theta = (T' - T_o')/(T_i' - T_o'). \tag{3}$$

Equations (1b) and (1d) are cross-differentiated and combined. Using the following definitions of ψ, Γ and ζ

$$u = -(1/r)\,\partial\psi/\partial z \tag{4a}$$

$$w = (1/r)\,\partial\psi/\partial r \tag{4b}$$

$$\zeta = \partial u/\partial z - \partial w/\partial r \tag{4c}$$

$$\Gamma = rv \tag{4d}$$

the non-dimensional differential equations are:

$$\begin{aligned}\partial\zeta/\partial t + \partial(u\zeta)/\partial r - (2\Gamma/r^3)\,\partial\Gamma/\partial z + \partial(w\zeta)/\partial z &+ (GrFr/Re^7)(\Gamma/r^3)(2\theta\partial\Gamma/\partial z + \Gamma\partial\theta/\partial z) \\ &- (1/Re)[\partial^2\zeta/\partial r^2 + \partial^2\zeta/\partial z^2 + (\partial\zeta/\partial r)/r \\ &- \zeta/r^2] - (Gr/Re^2)\,\partial\theta/\partial r = 0\end{aligned} \tag{5a}$$

$$\begin{aligned}\partial\Gamma/\partial t + [\partial(ru\Gamma)/\partial r]/r + \partial(w\Gamma)/\partial z &- (GrFr/Re^2)u\theta\Gamma/r^2 - (1/Re)[\partial^2\Gamma/\partial r^2 \\ &- (\partial\Gamma/\partial r)/r + \partial^2\Gamma/\partial z^2] = 0\end{aligned} \tag{5b}$$

$$\zeta = (-1/r)[\partial^2\psi/\partial z^2 + \partial^2\psi/\partial r^2 - (\partial\psi/\partial r)/r] \tag{5c}$$

$$\begin{aligned}\partial\theta/\partial t + u\partial\theta/\partial r + w\partial\theta/\partial z &= (1/PrRe)[(\partial\theta/\partial r)/r \\ &+ \partial^2\theta/\partial r^2 + \partial^2\theta/\partial z^2].\end{aligned} \tag{5d}$$

2.2. *The boundary conditions*

Each boundary has been assumed to be impermeable and isothermal (different boundaries have different temperatures), and either moving at a constant angular velocity or stationary. The two cases considered are described in Table 1. Case U is chosen to simulate the upper annulus while Case L represents the lower annulus.

Table 1. Boundary conditions for temperature θ and angular velocity Ω

Case	Boundary			
	$r = r_i$	$r = r_o$	$z = 0$	$z = H$
U	$\Omega = 1$ $\theta = 1$	$\Omega = 0$ $\theta = 0$	$\Omega = 0$ $\theta = 0$	$\Omega = 1$ $\theta = 1$
L	$\Omega = 1$ $\theta = 1$	$\Omega = 0$ $\theta = 0$	$\Omega = 1$ $\theta = 1$	$\Omega = 0$ $\theta = 0$

At any boundary

$$\psi_b = \text{constant and } (\partial\psi/\partial n)_b = 0 \quad (6)$$

where n is the normal coordinate. In a simply-connected closed system the value of ψ_b is arbitrary and is taken as zero.

The boundary condition for the swirl velocity Γ is

$$\Gamma_b = r^2\Omega_b. \quad (7)$$

From equations (5c) and (6), the boundary vorticity ζ_b is

$$\zeta_b = -1/r(\partial^2\psi/\partial n^2)_b. \quad (8)$$

The numerical implementation of this is an extension of the Woods formula [8]. At $r = r_i$, for example, it becomes

$$\zeta_b = -3\psi_2/[\Delta r^2(r_i + \Delta r/4)] - \zeta_2(r_i/2 + \Delta r/4)/(r_i + \Delta r/4) \quad (9)$$

in which the subscript 2 refers to the first internal mesh point.

3. SOLUTION PROCEDURE

The finite-difference forms of the dimensionless differential equations use central difference formulae for spatial derivatives, and a forward difference formula for the time derivatives. The resulting equations were solved by the Samarskii–Andreyev ADI scheme [9] using the false-transient technique [10], chosen for its fast rate of convergence. This technique involves the introduction of a fictitious time derivative $\partial\psi/\partial t$ to equation (5c), and a relaxation factor to the time derivatives in all equations. These factors can be adjusted to under- or over-relax the computations as necessary to achieve and to accelerate convergence.

The number of grid nodes for the geometry with $A = 0.5$, 1.0 and 2.0 were 31 in each of r and z directions. However, for $A = 0.25$, 61 nodes in the r direction and 16 in the z direction were used; for $A = 4.0$, these numbers of nodes were interchanged. An attempt has been made to choose the number of nodes in such a way that the resulting grids were of approximately square shape; this was found useful for achieving higher accuracy.

The converged solutions reported herein took, in general, from about 100 to 2000 iterations; the CPU time per iteration was about 1.3 s on a CDC Cyber 171. The convergence criterion used was that the sum over the entire domain of the difference between the current value of each dependent variable and that in the previous iteration, normalized with the maximum value of the variable, was $\leqslant 10^{-3}$.

* Not all possible combinations were used.

4. RESULTS AND DISCUSSIONS

Numerical results were computed for the following values of the relevant parameter:*

R = 1.2, 1.5, 2.0, 4.0 and 8.0
A = 0.25, 0.5, 1.0, 2.0 and 4.0
Ra = 10^3, 10^4 and 10^5
Re = 10, 25, 50, 75, 100, 150, 200, 250 and 300.

All solutions were found for $Pr = 0.7$ and $Fr = 0$. The latter condition was chosen because numerical calculations [1] had indicated that the solutions studied here in the aforementioned ranges of Ra and Re are independent of Fr. This assumption eliminates the buoyant component of the centrifugal and Coriolis accelerations [see equation (5)].

4.1. *Flow structure*

4.1.1. *Upper annulus.* The major forces which determine the flow pattern in the upper annulus are: (1) the gravitational buoyancy force [$Gr/Re^2\,\partial\theta/\partial r$ in equation (5a)] which causes the fluid to rise along the inner cylinder and move outwards along the upper boundary, and (2) the centrifugal force [$2\Gamma/r^3\,\partial\Gamma/\partial z$ in equation (5a)] which pushes the fluid outwards from the inner cylinder along the rotating bottom surface, thereby creating an opposing motion. Because of the opposing effects of these forces, if one is much stronger than the other, a monocellular flow pattern would be generated. However, when these forces are of the same order of magnitude, a two- or three-cell flow pattern will be found. Some of the many computed flow patterns are presented in Figs. 2–6. The axis of the annulus is located off the left-hand side of each diagram, which shows the right-hand half of a vertical cross-section of the annulus.

The effects of variation of R on the flow pattern for constant A, Ra and Re is shown in Fig. 2. An increase in the radius ratio R brings the cavity closer to the axis of the annulus and diminishes the influence of the centrifugal force. As a result, the counterclockwise (centrifugally dominated) flow is changed to a clockwise (buoyancy dominated) flow through a succession of multicellular flow patterns. The maximum and minimum values of the stream function for the various cases, shown in these diagrams, suggest that the original centrifugally driven cell of Fig. 2a loses momentum as the natural convective cell is developed; the resulting buoyancy driven flow of Fig. 2e is an order-of-magnitude weaker than that of Fig. 2a. This reduction in the values of the stream function is believed to be due to the counter effects of these opposing cells, which is also reflected in the CPU time required to achieve convergence: the cases with multicellular flow patterns took, in general, three to six times more iterations than the monocellular flows.

Figure 3 shows the flow structure for various values of A, keeping R, Ra and Re constant. By increasing A, the area of the heated inner cylinder which gives

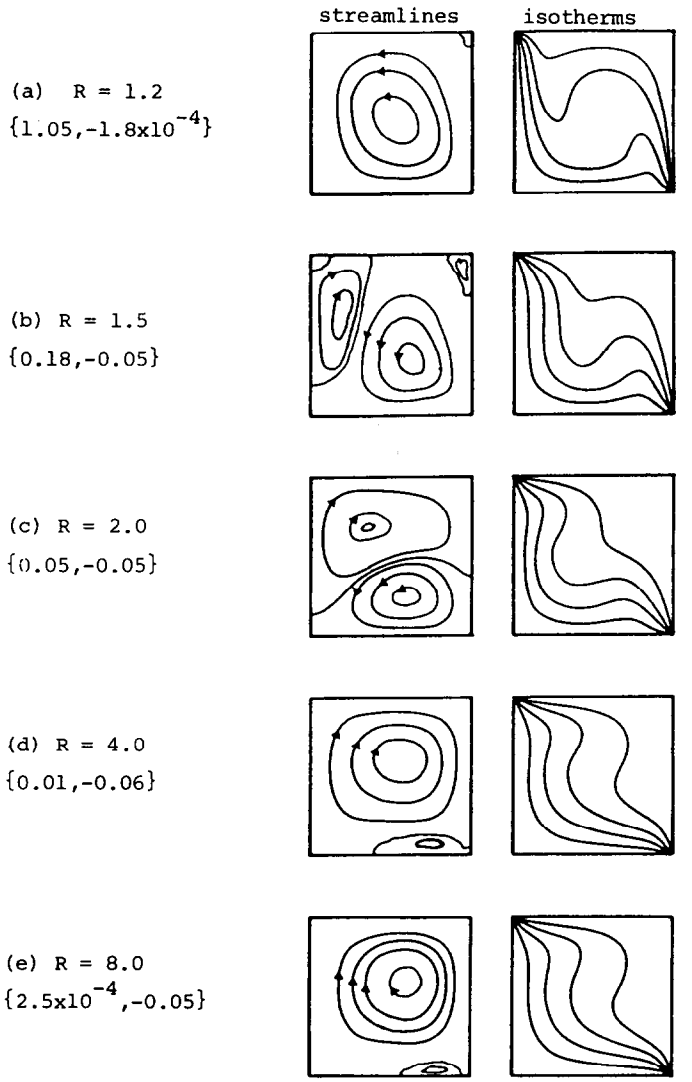

FIG. 2. Streamlines and isotherms for the upper annulus at $Re = 10^2$, $Ra = 10^4$ and $A = 1.0$. Numbers within { } represent the maximum and minimum stream function values, respectively.

rise to the buoyancy force increases. As it can be seen in Fig. 3, the counterclockwise flow structure is changed to a mostly clockwise flow pattern by increasing A from 0.25 to 4.0. Apparently, increasing R from 1.2 to 8.0 (about seven-fold) produces a larger change in the flow pattern than the 16-fold increase in A; however, the same increase in A results in an increase in the ψ values whereas the seven-fold increase in R produces a decrease in the stream functions.

In order to study the influence of Re and Ra on the flow structures, a single geometry with $A = 0.25$ and $R = 2.0$ has been considered. Figures 4–6 show the streamlines for this geometry. In Fig. 4a, the flow field for $Re = 10$ and $Ra = 10^3$ shows the combined influence of the buoyancy and centrifugal forces. The central counterclockwise cell is due to the centrifugal force whereas the clockwise cells at the ends of the cavity are due to the buoyancy forces generated by the horizontal temperature gradient near each end of the cavity, i.e. by the heat transferred from the heated inner cylinder to the cooled upper wall, and from the heated lower wall to the cooled outer cylinder. The cell near the outer cylinder is stronger than the other two cells. Although this seems puzzling, a calculation indicates that the heated area available to drive the cell near the outer cylinder is larger than that for the cell near the inner cylinder (assuming the cells are of equal size); the relative difference in the strength of these cells is a function of R: the larger is R, the stronger is the cell near the outer cylinder. As Re is increased (Fig. 4b), the clockwise eddies disappear and the centrifugal force dominates the field.

For $Re = 10$ and $Ra = 10^4$ (Fig. 5a), the influence of natural convection increases as reflected by the size of the clockwise cells and the magnitude of the stream functions; the counterclockwise cell is comparatively weak and at the verge of disappearance. However, an increase of Re enhances the centrifugal

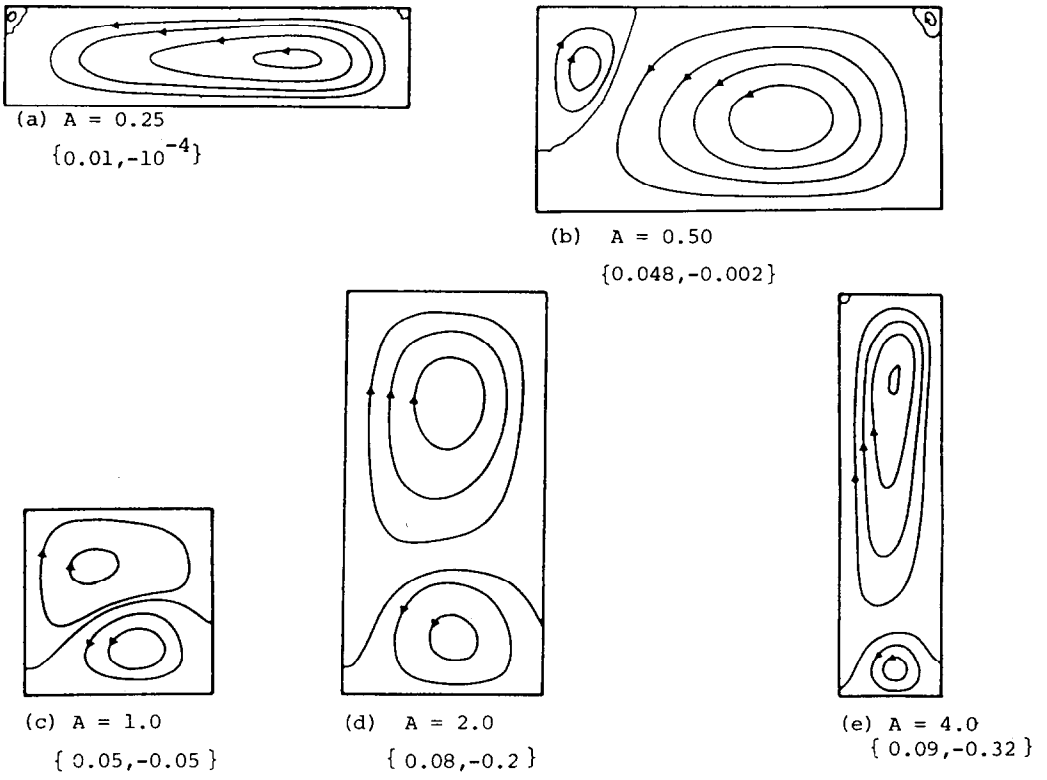

FIG. 3. Streamlines for the upper annulus at $Re = 10^2$, $Ra = 10^4$ and $R = 2.0$.

force and this cell subsequently dominates the flow field (Fig. 5b). The flow patterns for $Ra = 10^5$ are shown in Fig. 6. For $Re = 10$ (Fig. 6a), the natural convective eddies are stronger than the centrifugal cell. The stream function values and patterns remain unchanged when Re is increased to 100. However, for $Re = 300$ (Fig. 6b), the flow is generally due to the centrifugal effects. Comparison of the flow patterns for a constant Re and the various values of Ra indicates the increasing influence of natural convection as Ra changes from 10^3 to 10^5.

In general, increasing Ra and/or A and/or R strengthens the buoyancy-driven cells while an increase in Re promotes the dominance of the flow field by the centrifugal force.

It was mentioned earlier that the solutions for the cases with multicellular flow patterns are found to require more computer time than the monocellular flow problems to achieve convergence. For example, the solution presented in Fig. 2b took about 2700 iterations as compared with Fig. 2a which converged after 338 iterations. It is believed that the numerical difficulty encountered in obtaining a converged solution for the former case is due to the extreme sen-

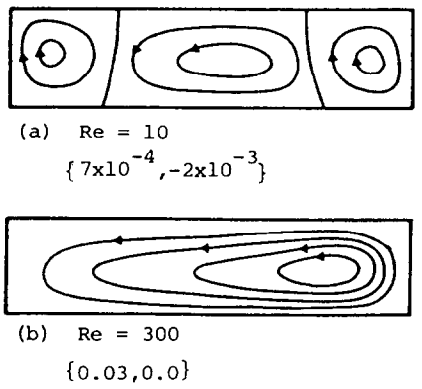

FIG. 4. Streamlines for the uper annulus for $Ra = 10^3$, $A = 0.25$ and $R = 2.0$.

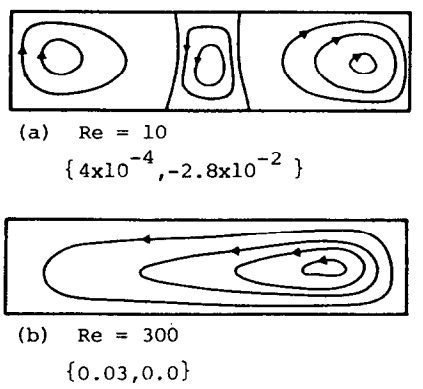

FIG. 5. Streamlines for the upper annulus at $Ra = 10^4$, $A = 0.25$ and $R = 2.0$.

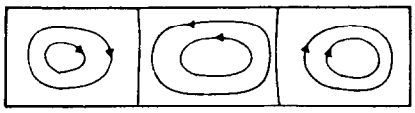

(a) Re = 10

{0.12,-0.4}

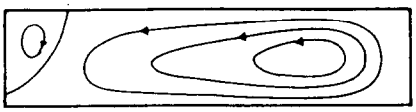

(b) Re = 300

$\{0.03,-1.5\times10^{-3}\}$

FIG. 6. Streamlines for the upper annulus at $Ra = 10^5$, $A = 0.25$ and $R = 2.0$.

sitivity of the flow to the opposing and almost equal forces, and to the transient nature of the solution process. An increase in Ra ($Ra = 3 \times 10^4$) resulted in a converged solution in 365 iterations with a single clockwise cell. Similar problems in obtaining a converged solution were also encountered with the case of $A = 1.0$ and $R = 1.2$ at the point of transition of the flow from clockwise to counterclockwise.

Converged solutions could not be obtained at $Ra = 10^5$ for $A = 1.0$ and $R \geqq 8.0$ at $Re > 150$; or for $A = 4.0$ and $R = 2.0$ at $Re = 300$. This is thought to be due to the instability in the flow field which may have been caused by the inception of the transition of the flow from laminar to turbulent regime; the present study considers laminar flows only.

4.1.2. *Lower annulus.* Unlike the upper annulus, the centrifugal and buoyancy forces in the lower annulus are supportive, giving rise to a clockwise flow field of one or two cells. The two-cell flow fields are generally found for low Re with extreme values of A (i.e. $Re = 10$ and $A = 0.25$ or 4.0); an almost stagnant region was seen to exist between the cells. At higher values of Re, however, the two cells were found to have merged, creating a single eddy pattern. Figures 7 and 8 show the flow patterns for a few of the cases studied here.

No significant change in the streamlines of Figs. 7a and b is apparent as R is increased from 1.2 to 8.0 (at $Re = 100$ and $Ra = 10^4$) except for the shift of the centre of rotation towards the upper right corner creating a nearly stagnant region near the lower plate; this change of R reduces the values of the stream function by an order of magnitude. Figures 7c and d show the effect of variation of A on the flow field. As A is increased from 0.25 to 4.0, the basic flow pattern remains unchanged while an order-of-magnitude increase in the stream function is observed. Because of the high value of A in Fig. 7d, the fluid near the lower plate is almost stationary.

The two-cell flow fields mentioned earlier are shown in Fig. 8a; both eddies are moving in the same direction (clockwise), creating a very slow moving fluid region in between. By increasing Re, the two cells merge and form a single eddy structure, as shown in Fig. 8b. It is believed that by reducing R a similar

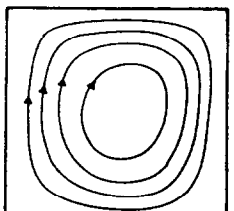

(a) A = 1.0, R = 1.2

{0.0,-0.9}

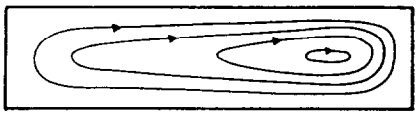

(c) R = 2.0, A = 0.25

{0.0,-0.012}

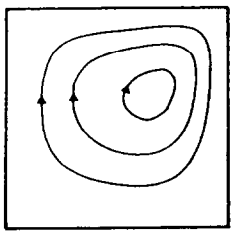

(b) A = 1.0, R = 8.0

{0.0,-0.03}

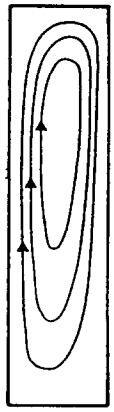

(d) R = 2.0, A = 4.0

{0.0,-0.28}

FIG. 7. Streamlines for the lower annulus at $Re = 10^2$ and $Ra = 10^4$.

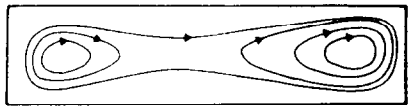

(a) Re = 10, Ra = 10^3

{0.0,-0.0036}

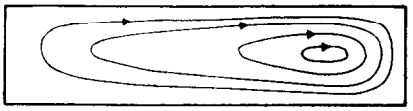

(b) Re = 300, Ra = 10^3

{0.0,-0.03}

FIG. 8. Streamlines for the lower annulus with $A = 0.25$ and $R = 2.0$.

change in the flow pattern can be found. The flow patterns of Figs. 8a and b did not significantly change (except for the value of ψ) when Ra was increased to 10^5.

It is interesting to note that by increasing Re from 10 to 300 at $Ra = 10^3$, an order-of-magnitude rise in the maximum stream function (ψ_{max}) is observed. In contrast, such an increase in Re at $Ra = 10^5$, reduces ψ_{max} by an order-of-magnitude. An examination of all of the solutions for the lower annulus indicates that in most cases ψ decreases with Re; this pattern has also been reported in ref. [1]. Although this is contrary to what is expected, it should be noted that ψ has been non-dimensionalized by $L'^3\Omega' = ReL'\nu'$. Therefore, when ψ decreases with Re, it does not necessarily imply a decrease in ψ', the dimensional stream function. For example, assuming $L'\nu'$ remains unchanged, ψ'_{max} for the case depicted in Fig. 8b ($Re = 300$) is, in fact, 3.6 times greater than that shown in Fig. 8a ($Re = 10$). Hence, an increase in Re is accompanied with a rise in the flow rate. This point is further substantiated by the rise in Nu_L (not reported here for the sake of conciseness) found in this study.

4.2. *Heat transfer*

The parameter of practical importance in the thermal design of electric motors is the heat transfer, which is measured by the average Nusselt number, $\overline{Nu}$. Using i, o, t and b to refer to the inner, outer, top and bottom surfaces of the cavity respectively, $\overline{Nu}$ can be computed by

$$\overline{Nu}_{\underset{(t)}{b}} = -2(R-1)/(R+1)\int_{r_i}^{r_o}(\partial\theta/\partial z)_{\substack{z=0\\(z=A)}} r\,dr \qquad (10a)$$

$$\overline{Nu}_{\underset{(o)}{i}} = (-1/A)\int_0^A (\partial\theta/\partial r)_{\substack{r=r_i\\(r=r_o)}} dz \qquad (10b)$$

where

$$\overline{Nu}_j = \bar{h}'_j L'/k' \qquad (10c)$$

on any surface j and

$$\bar{h}'_j = -k'_j/\{(T'-T'_o)S'_j\}\int_{S'_j}(\partial T'/\partial n')_j dS'_j. \qquad (11)$$

The total heat transferred from the hot surfaces to the cold surfaces (which must be equal) for each of the upper and lower annuli can be found by calculating the total average Nusselt number given below:

For hot surfaces:

$$\overline{Nu}_{\underset{(L)}{U}} = [A/(R-1)]\overline{Nu}_i + [(R+1)/(R-1)/2]\overline{Nu}_{\underset{(t)}{b}}. \qquad (12a)$$

For cold surfaces:

$$\overline{Nu}_{\underset{(L)}{U}} = [RA/(R-1)]\overline{Nu}_o + [(R+1)/(R-1)/2]\overline{Nu}_{\underset{(b)}{t}}. \qquad (12b)$$

$\overline{Nu}_U$ and $\overline{Nu}_L$ are based on $\bar{h}$ which is formulated to depend on a fictitious area of $2\pi L'^2$ and the temperature difference of $(T'_i - T'_o)$. The overall heat transfer from the electric motor ($\overline{Nu}_T$) is the algebraic sum of $\overline{Nu}_U$ and $\overline{Nu}_L$.

In order to see the effects of geometry on heat transfer, $\overline{Nu}_i$ and $\overline{Nu}_b$ for the upper annulus at $Re = 10^2$ and $Ra = 10^4$ with various values of A and R are plotted in Fig. 9. $\overline{Nu}_i$, in general, decreases at first and then very slowly increases with increasing R; however, increasing A results in a decrease in heat transfer except for $A > 1$ where a rise in A is accompanied by higher $\overline{Nu}_i$ when $R > 3.0$. This behaviour is compatible with the flow structures for the various cases: for $A \leqq 1$, the flow changes from a predominantly monocellular pattern to a multicellular structure by increasing R; whereas for $A > 1$, this change in the flow pattern is reversed. The multicellular flows are less efficient in transferring heat due to the opposing direction of the eddies which thickens the thermal boundary layer and thus reduces the temperature gradient and heat transfer. The trend exhibited by $\overline{Nu}_b$ in Fig. 9 is self-explanatory: it consistently increases with increasing R and decreasing A except at high values of A where $\overline{Nu}_b$ is almost independent of A.

The total heat transfer for the upper annulus for various values of A and R are given in Fig. 10. $\overline{Nu}_U$ (solid lines) decreases with increasing R and decreasing A when $A \geqq 1$ and increasing A when $A < 1$, except for the $R = 1.2$ case; $\overline{Nu}_L$ profiles (not shown in Fig. 10) are virtually the same as those for $\overline{Nu}_U$. The overall heat transfer, $\overline{Nu}_T$ (broken lines), shows a very similar trend. The effect of reducing R from around 4 to 1.2 on $\overline{Nu}_T$ is almost a 10-fold increase while that due to increasing A from 1.0 to 4.0 is comparatively very small.

$\overline{Nu}_i$ and $\overline{Nu}_b$ curves for other values of Ra and Re showed similar trends to those given in Fig. 9 and therefore will not be repeated here; these results are available in ref. [11]. However, the overall heat trans-

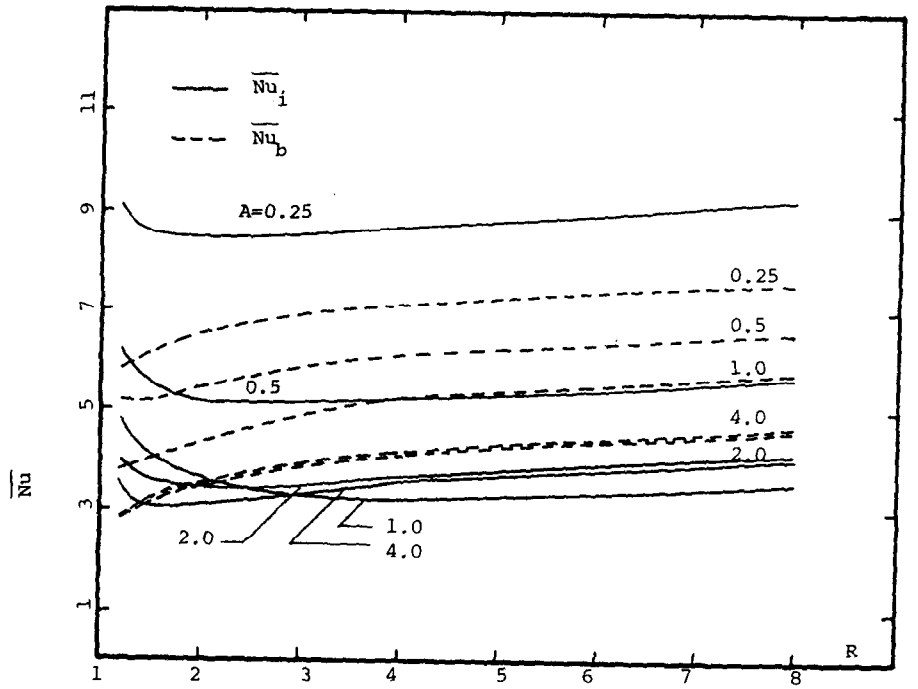

FIG. 9. Nusselt number distribution for the inner and bottom surfaces for the upper annulus of various sizes at $Re = 10^2$ and $Ra = 10^4$.

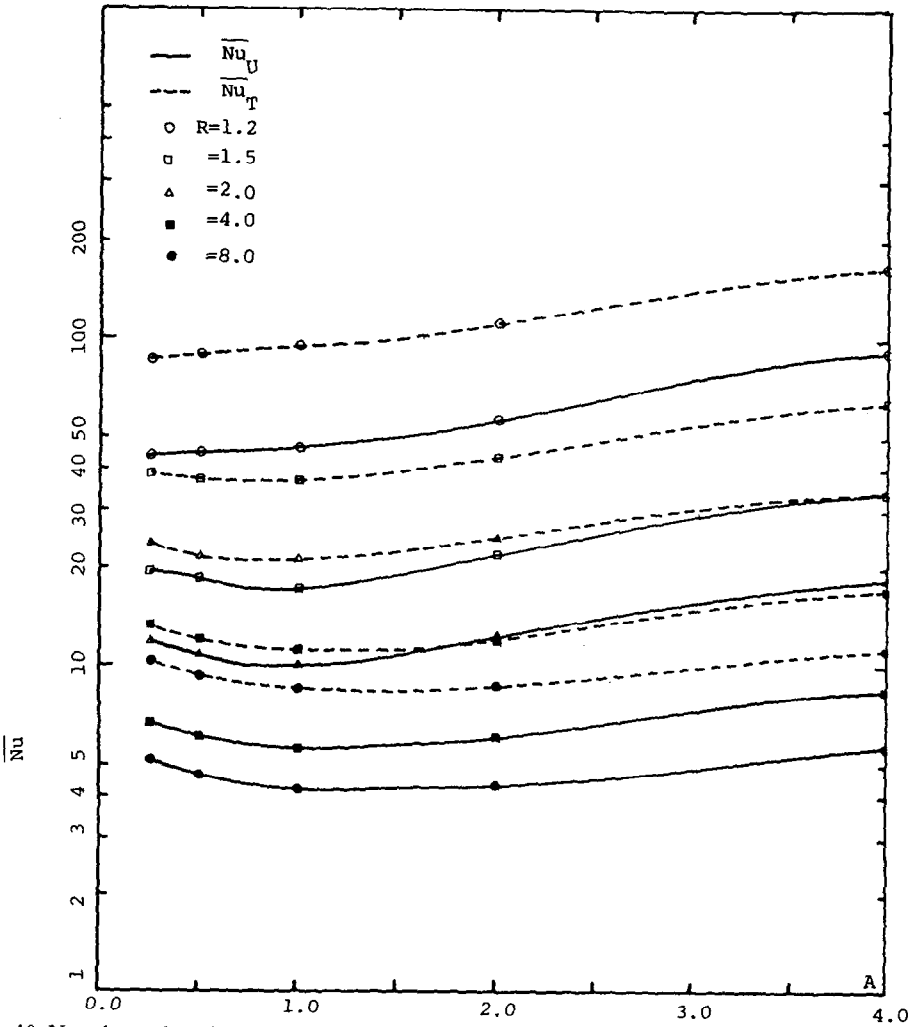

FIG. 10. Nusselt number distribution for the upper annulus of various sizes at $Re = 10^2$ and $Ra = 10^4$.

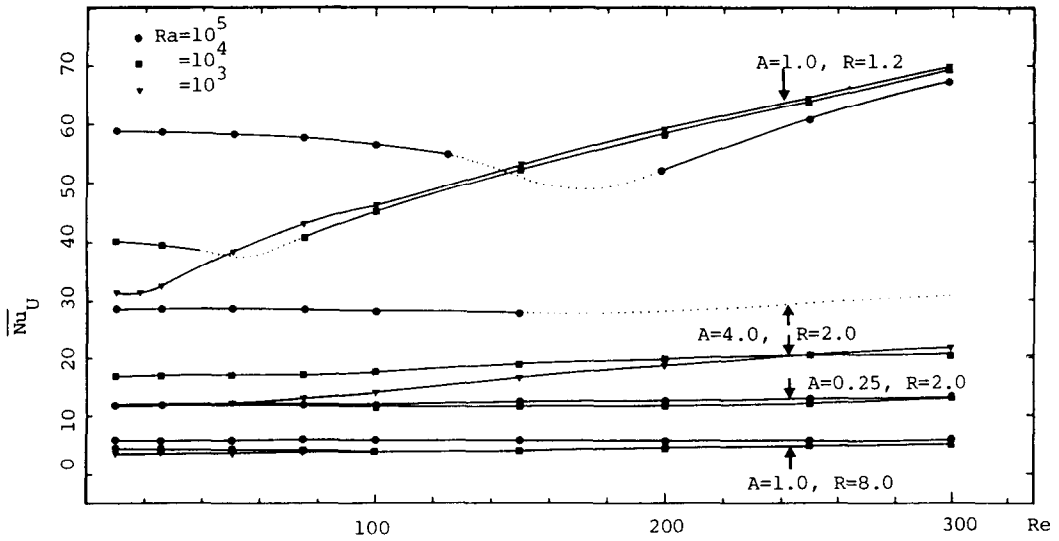

FIG. 11. $\overline{Nu}_U$ distribution for various values of A, R, Re and Ra.

fer data for the upper annulus are plotted in Fig. 11. It is evident that an increase in both Ra and Re is accompanied by a rise in the heat transfer. At higher values of Re, the influence of natural convection diminishes as the different Ra curves converge to a single line for each geometry.

The drop in $\overline{Nu}_U$ which is apparent in the $\overline{Nu}$ profiles of Fig. 11, especially for $A = 1.0$ and $R = 1.2$, is due to the interaction of the buoyancy and centrifugal forces. $\overline{Nu}_U$ is minimum when the natural convective clockwise cell is changed as a result of an increase in Re to a centrifugally driven counterclockwise flow; similar profiles are reported in ref. [1] for $A = 1.0$ and $R = 2.0$. The decrease in $\overline{Nu}_U$ for $A = 1.0$ and $R = 1.2$ is more pronounced because this reversal of the direction of the flow takes place over a comparatively narrower range of Re; for other geometries, the transition requires a significant increase in Re and, therefore, a wider range which is not covered here. For geometries with large values of R, the inner cylinder is much smaller than the outer one and therefore the influence of rotation is not very significant.

The difference between the heat in and out of the system for both upper and lower annuli was found to increase with the radius ratio; the discrepancy was calculated to be mostly under 10%. Further mesh refinement would provide a better energy balance.

A plot of $\overline{Nu}_T$ for the solutions obtained in this study are given in Fig. 12. The shape of the $\overline{Nu}_T$ profile is very similar to that for $\overline{Nu}_U$ but the values of the former are about twice as large as those of the latter since $\overline{Nu}_U$ is approximately the same as $\overline{Nu}_L$ despite the difference in the flow patterns for the upper and lower annuli which were reported earlier.

The data presented in Fig. 9 show that the variation in $\overline{Nu}$ profiles due to changes in A, R, Ra and Re is not very significant. However, the local heat transfer profiles given in Fig. 13 show that the motor experiences very high temperature gradients at the ends of the rotor and at the edges of the heated horizontal surfaces. Therefore, for design purposes, a knowledge of the local heat transfer distribution is necessary. A motor with homogeneous physical properties may fail when exposed to such variable thermal conditions; this cannot be accounted for if only average heat transfer data were available. It should be added that the significant variation in the Nu_i values of Fig. 13 can be explained by the flow structures of the various cases presented earlier in Fig. 2; the monocellular flow driven by the centrifugal force (Fig. 2a) is more efficient than those generated by the buoyancy force (Fig. 2e) and by buoyancy and centrifugal forces (Fig. 2d). However, no large variation in Nu_b by varying R is observed as shown in Fig. 13b.

An attempt has been made to correlate all of the heat transfer data obtained in this study. Different equations were found to be necessary to describe properly the heat transfer for the various surfaces and geometries as shown in Figs. 9–13; for the sake of conciseness, these equations will not be discussed here. However, a single correlation equation of the general form given below was developed here to calculate the heat transfer for design purposes:

$$\overline{Nu} = c_1 Re^{c_2} Gr^{c_3}[1 + |A-1|]^{c_4}(R-1)^{c_5}. \quad (13)$$

The values of the constants c_1–c_5 for $\overline{Nu}_U$, $\overline{Nu}_L$ and $\overline{Nu}_T$ are listed in Table 2.

Table 2. Constants c_1–c_5 in equation (13)

	c_1	c_2	c_3	c_4	c_5
$\overline{Nu}_U$	1.000	0.148	0.206	0.218	−0.669
$\overline{Nu}_L$	1.000	0.165	0.197	0.187	−0.670
$\overline{Nu}_T$	1.000	0.195	0.254	0.224	−0.669

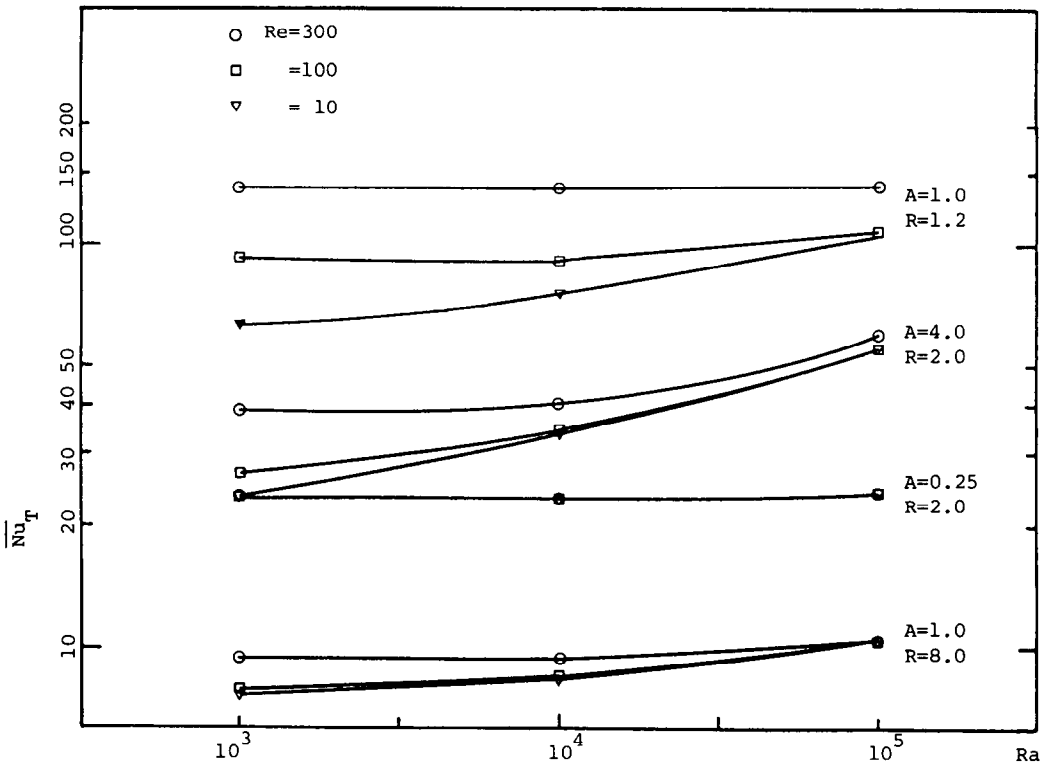

FIG. 12. $\overline{Nu}_T$ distribution for various values of A, R, Ra and Re.

The set of equations described by equation (13) and Table 2 is in general agreement with the heat transfer profiles of Figs. 10 and 12, i.e. $\overline{Nu}$ increases with both Ra and Re, and decreases with increasing R and decreasing A when $A < 1$ and increasing A when $A > 1$. In order to show the scatter of the numerical heat transfer data around equation (13), $\overline{Nu}_T$ found in this study and those calculated by equation (13) are plotted vs the right-hand side of this equation in Fig. 14. As it can be seen, no general pattern between the different sets of data is apparent which shows the degree of complexity of the development of a single correlation equation that can accurately represent these data. However, the above equations are considered to be reasonably accurate for estimating the heat transfer in the design of vertical rotating annuli at this time.

5. CONCLUSIONS

Numerical heat transfer profiles and flow patterns were found for various rotating vertical annular cavities in the ranges $0.25 \leqq A \leqq 4.0$, $1.2 \leqq R \leqq 8.0$, $10 \leqq Re \leqq 300$ and $10^3 \leqq Ra \leqq 10^5$. It was found that the flow pattern in the upper annulus is determined by the relative magnitude of the gravitational buoyancy and centrifugal forces: if either of the forces is dominant, a monocellular pattern was found; otherwise the flow structure was multicellular. For low values of R and high values of Re, the centrifugal force was predominant and a counterclockwise flow existed. On the other hand, for high values of A and Ra, a clockwise flow structure generated by the buoyancy force was found to exist. For the lower annulus, both forces generated a clockwise flow field of one- or two-cell structures; the latter pattern was found only for the cases with extreme values of A.

The heat transfer profiles did not reveal a significant change in $\overline{Nu}$ values for the various surfaces when R was varied at constant Ra and Re; variation in A, however, produced a three-fold change in $\overline{Nu}$. In contrast, $\overline{Nu}_T$ was found to decrease by an order of magnitude when R was changed from 1.2 to 8.0. $\overline{Nu}_T$ was found to increase with decreasing A when $A < 1$ and with increasing A when $A > 1$, but not as strongly as with decreasing R. Increasing Ra and/or Re, in general, produced higher heat transfer, in agreement with the general theory of convective flows.

Profiles of local Nu showed a high heat flux and consequently temperature gradient at the ends of the rotor and the edges of the horizontal planes, thereby creating non-uniform heat transfer distributions. Hence computations of these local heat transfer fields are necessary for the better design of the electric motors.

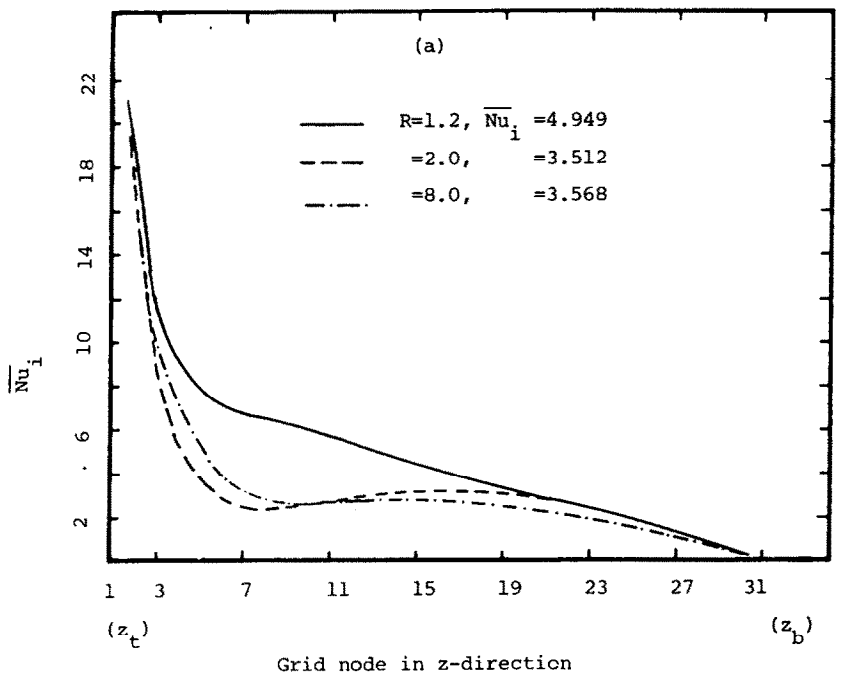

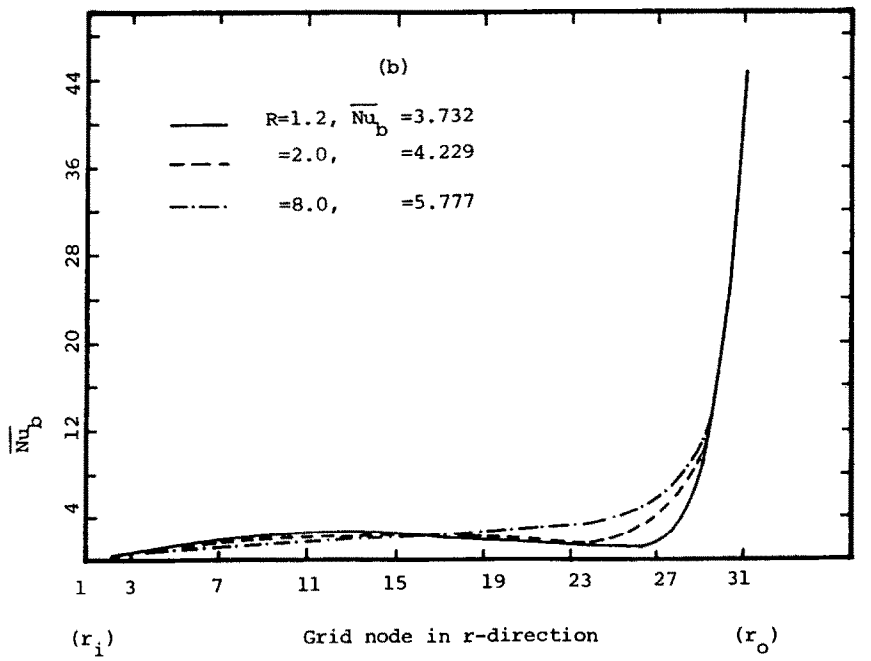

FIG. 13. Local *Nu* distribution for the upper annulus at $Re = 10^2$, $Ra = 10^4$ and $A = 1.0$.

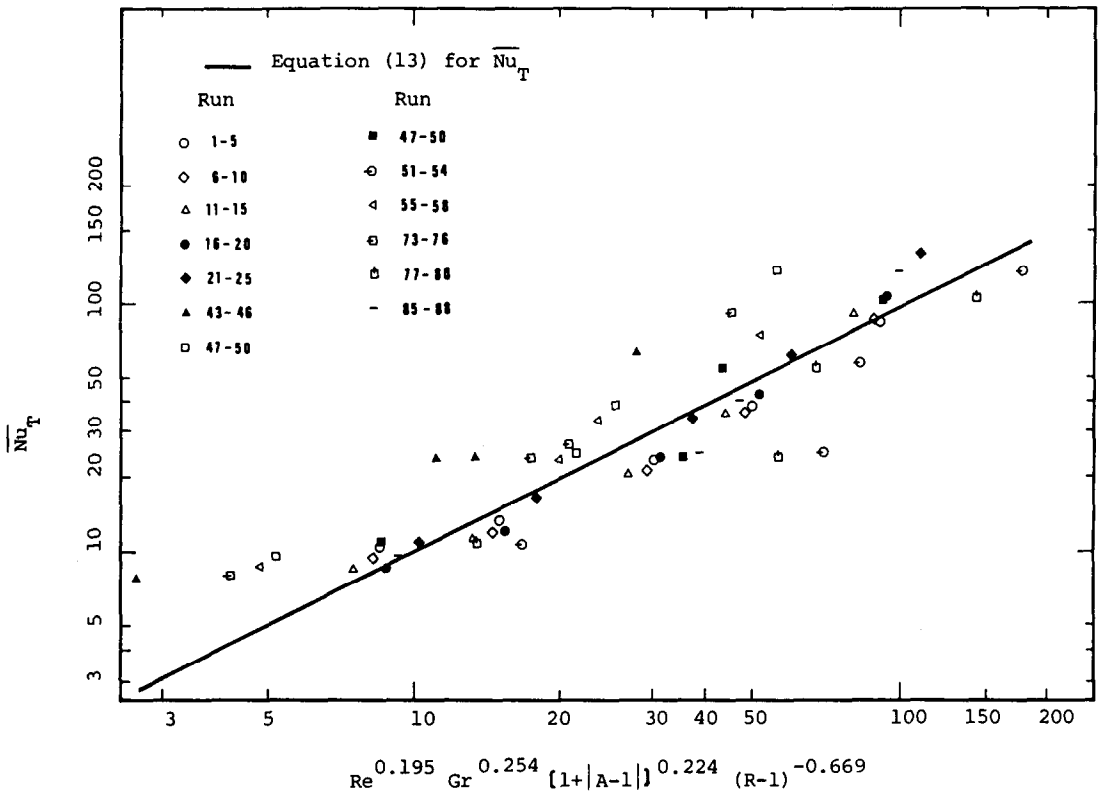

FIG. 14. Comparison between the present numerical heat transfer data and those found via equation (13).

REFERENCES

1. G. de Vahl Davis, E. Leonardi and J. A. Reizes, Convection in a rotating annular cavity. In *Heat and Mass Transfer in Rotating Machinery* (Edited by D. E. Metzger and N. H. Afgan), pp. 131–142. Hemisphere, Washington, DC (1984).
2. A. T. Conlisk and J. D. A. Walker, Forced convection in a rapidly rotating annulus, *J. Fluid Mech.* **122,** 91–108 (1982).
3. M. Singh and S. C. Rajvanshi, Heat transfer between rotating eccentric cylinders with different radii, *Int. J. Heat Mass Transfer* **25,** 1719–1724 (1982).
4. K. Buhler and H. Oertel, Thermal cellular convection in rotating rectangular boxes, *J. Fluid Mech.* **114,** 261–282 (1982).
5. M. Charmchi and E. M. Sparrow, Analysis of natural convection in the space between concentric vertical cylinders of different height and diameter, *Numer. Heat Transfer* **5,** 119–144 (1982).
6. E. M. Sparrow and M. Charmchi, Natural convection experiments in an enclosure between eccentric or concentric vertical cylinders of different height and diameter, *Int. J. Heat Mass Transfer* **26,** 133–143 (1983).
7. M. F. Young and T. R. Ulrich, Mixed convection heat transfer from a vertical heated cylinder in a crossflow, *Int. J. Heat Mass Transfer* **26,** 1889–1892 (1983).
8. L. C. Woods, A note on the numerical solution of fourth order differential equations, *Aeronaut. Q.* **5,** 176–187 (1954).
9. A. A. Samarskii and V. B. Andreyev, On a high accuracy difference scheme for elliptic equations with several space variables, *U.S.S.R. Comp. Math. Math. Phys.* **3,** 1373–1382 (1963).
10. G. D. Mallinson and G. de Vahl Davis, The method of the false transient for the solution of coupled elliptic equations, *J. Comp. Phys.* **12,** 435–461 (1973).
11. M. A. Hessami, G. de Vahl Davis, E. Leonardi and J. A. Reizes, Mixed convective heat transfer and flow patterns in vertical cylindrical annuli—a parametric study, Report No. 1986/FMT/1, School of Mechanical and Industrial Engineering, University of New South Wales, Kensington, NSW, Australia (1986).

CONVECTION MIXTE DANS UN ESPACE ANNULAIRE VERTICAL

Résumé—On étudie numériquement les configurations d'écoulement laminaire et le transfert thermique pour de l'air enfermé dans une enceinte par deux cylindres concentriques et verticaux et deux plans horizontaux. Le cylindre intérieur et un des plans horizontaux sont chauffés et tournent autour de l'axe vertical; l'autre plan et le cylindre extérieur sont refroidis et sont fixes. Cette géométrie simule l'espace entre les extrémités du rotor, d'un petit moteur électrique refroidi par air et monté verticalement. Les résultats facilitent la conception d'un tel moteur. On a étudié les influences de la géométrie (rapport des rayons R et rapport de forme A), de Ra et Re sur les distributions de température et de vitesse. Des solutions sont obtenues pour $0{,}25 \leqslant A \leqslant 4$, $1{,}2 \leqslant R \leqslant 8$, $10 \leqslant Re \leqslant 300$ et $10^3 \leqslant Ra \leqslant 10^5$. On a trouvé que pour les valeurs faibles de R et les grandes valeurs de Re, l'écoulement est dominé par les forces centrifuges, tandis que pour A et Ra grand les effets gravifiques déterminent les configurations d'écoulement et, par suite, le transfert thermique. Des configurations monocellulaires ont été trouvées dans les cas où l'une de ces forces est dominante; autrement on obtient des structures à deux ou trois cellules.

GEMISCHTE KONVEKTION IN VERTIKALEN ZYLINDRISCHEN RINGSPALTEN

Zusammenfassung—Die laminaren Strömungsformen und die Wärmeübertragung in dem luftgefüllten Spalt zwischen zwei vertikalen, konzentrischen Rohren und zwischen zwei horizontalen Ebenen wurde numerisch untersucht. Das innere Rohr und eine der horizontalen Ebenen sind beheizt und rotieren um ihre vertikale Achse; die andere horizontale Ebene und das äußere Rohr werden gekühlt und sind ortsfest. Diese geometrische Anordnung bildet die Spalte an den Enden des Rotors eines kleinen, luftgekühlten und vertikal befestigten Elektromotors nach. Die Ergebnisse erleichtern die Berücksichtigung thermischer Belange bei der Gestaltung eines solchen Motors. Der Einfluß der Geometrie (beschrieben durch das Radienverhältnis R und das Verhältnis A), der Rayleigh- und der Reynolds-Zahl auf Temperatur- und Geschwindigkeitsverteilung wurden untersucht. Man erhält Lösungen für $0.25 \leqslant A \leqslant 4.0$, $1.2 \leqslant R \leqslant 8.0$, $10 \leqslant Re \leqslant 300$ und $10^3 \leqslant Ra \leqslant 10^5$. Es ergibt sich, daß für niedere Werte von R und hohe Werte von Re die Strömung durch Zentrifugalkräfte beherrscht wird, während für großes A und Ra Auftriebseffekte die Strömungsformen und daher auch die Wärmeübertragung bestimmen. Einzellige Strömungsformen werden vorgefunden für die Fälle, bei denen eine dieser Kräfte vorherrschend ist; sonst erhält man zwei- oder dreizellige Strukturen.

СМЕШАННАЯ КОНВЕКЦИЯ В ВЕРТИКАЛЬНОМ ЦИЛИНДРИЧЕСКОМ КАНАЛЕ

Аннотация—Численно изучаются режимы ламинарного течения и теплообмена для воздуха, находящегося в замкнутом объеме, образованном двумя вертикальными концентрическими цилиндрами и двумя горизонтальными плоскостями. Внутренний цилиндр и одна из плоскостей нагреваются и вращаются вокруг вертикальной оси; другая горизонтальная плоскость и наружный цилиндр охлаждаются и остаются неподвижными. Такая геометрия моделирует зазоры на концах ротора небольшого вертикально установленного электродвигателя с воздушным охлаждением. Результаты используются при тепловом проектировании такого двигателя. Исследуется влияние геометрии (задаваемое отношением радиусов R и отношением высоты к ширине A), и чисел Ra и Re на распределения температуры и скорости. Получены решения для $0{,}25 \leqslant A \leqslant 4{,}0$, $1{,}2 \leqslant R \leqslant 8{,}0$, $10 \leqslant Re \leqslant 300$ и $10^3 \leqslant Ra \leqslant 10^5$. Найдено, что для малых значений R и больших Re на течение оказывают влияние центробежные силы, в то время как для больших A и Ra подъемные эффекты определяют режимы течения и теплообмена. В случаях с преобладанием указанных сил обнаружены одноячеистые режимы течения, в других случаях получены двух-или трехячеистые структуры.